Systematic multiparameter design methodology for an ultrasonic health monitoring system for full-scale composite aircraft primary structures

Ochôa, Pedro; Groves, Roger M.; Benedictus, Rinze

DOI
10.1002/stc.2340

Publication date
2019

Document Version
Final published version

Published in
Structural Control and Health Monitoring

Citation (APA)
Ochôa, P., Groves, R. M., & Benedictus, R. (2019). Systematic multiparameter design methodology for an ultrasonic health monitoring system for full-scale composite aircraft primary structures. *Structural Control and Health Monitoring*, *26*(5), Article e2340. https://doi.org/10.1002/stc.2340

Received: 3 September 2018 | Revised: 17 January 2019 | Accepted: 21 January 2019

DOI: 10.1002/stc.2340

RESEARCH ARTICLE

WILEY

Systematic multiparameter design methodology for an ultrasonic health monitoring system for full-scale composite aircraft primary structures

Pedro Ochôa[1,2] | Roger M. Groves[2] | Rinze Benedictus[1]

[1]Structural Integrity and Composites Group, Faculty of Aerospace Engineering, Delft University of Technology, Delft, The Netherlands

[2]Aerospace Non-Destructive Testing Laboratory, Faculty of Aerospace Engineering, Delft University of Technology, Delft, The Netherlands

Correspondence
Pedro Ochôa, Structural Integrity and Composites Group, Faculty of Aerospace Engineering, Delft University of Technology, Kluyverweg 1, 2629 HS Delft, The Netherlands.
Email: p.a.viegasochoadecarvalho@tudelft.nl

Funding information
Netherlands Enterprise Agency of the Ministry of Economic Affairs, Grant/Award Number: Thermoplastic Affordable Primary Aircraft Structures 2

Summary

The successful utilization of guided wave-based structural health monitoring (SHM) for detailed quantitative diagnostic of damage in composite aircraft primary structures depends on the excitation frequency, geometry, and positioning of the piezoelectric transducers. This study proposes a novel methodology to consistently define those parameters, which is not tuned for a single damage size, does not resort to unrealistic usage of pure guided wave modes, and is applicable to a generic full-scale composite aircraft primary structure. The proposed criteria for designing the piezoelectric transducer network are based on sensor output, coupled electro-mechanical response of the transducer-structure assembly, energy transfer from the bonded piezoelectric transducer to the structure, wavefront coverage of the monitored area, and measurement equipment capabilities. The design methodology was successfully validated by testing the capabilities of the SHM system for the diagnostic of barely visible impact damage of different severities, applied in different locations on a full-scale thermoplastic composite aircraft stiffened panel.

KEYWORDS

composite aircraft primary structure, experimental validation, structural health monitoring, system design, ultrasonic guided wave

1 | INTRODUCTION

The new generation of large commercial aircraft (e.g., Airbus A350, Boeing 787) has their main primary structures (fuselage, wings, and empennage) made of composites. It is difficult to obtain accurate fracture mechanics predictions for these materials, so regular inspection intervals cannot be reliably estimated, making the current maintenance paradigm unfeasible for airline fleets in the long term. This situation has led to the need for a change towards condition-based maintenance (CBM).[1-3] The implementation of CBM programmes depends on the capability of structural health monitoring (SHM) systems for assessing the integrity of a component during flight or in preflight checks.

In the last decades, research has shown that ultrasonic guided waves (GW) have a high potential for detailed quantitative damage diagnostic in thin-walled composite structures[4-6] especially because of their sensitive interaction with

incipient damage features such as barely visible impact damage (BVID) and delaminations, while propagating across relatively large areas. For GW based monitoring to be performed ultrasounds must be excited in the structure, and the only transducer technology that meets the requirements for SHM of fixed wing aircraft[7] and is capable of effectively accomplishing GW-based diagnostic is based on piezoelectricity.[8,9] Piezoelectric materials are mainly made from lead zirconate titanate (PZT) and can be produced in shapes and sizes, which are unobtrusive for the structure, can remain permanently installed, and can combine the functions of actuation and sensing.

The performance of PZTs as ultrasonic GW transducers for damage diagnostics depends on several key parameters that must be selected before installing the SHM system, namely, piezoelectric properties, geometry, excitation frequency content, and the network configuration (i.e., the relative position of the transducers within the area to be monitored). Usually, the excitation centre frequency is selected assuming the ideal scenario of pure guided mode excitation[10-12] or time-domain discrimination between guided modes,[13,14] after which a theoretically optimal dimension for the PZT transducer can be found from the wavelength tuning effect.[15-17] Another criterion for choosing the excitation centre frequency is to match the minimum resolvable distance by a certain pure guided mode with the minimum size of the damage to be detected.[18] When it comes to transducer placement, it is common to either use a high density network around a confined region (less than half metre) within the larger critical area[19-21] or to mathematically optimize the configuration for detecting specific damage scenarios/sizes.[22] For a preliminary level of optimization, the necessary parametric studies can be conducted efficiently by solving the two-dimensional analytical wave equations with externally incorporated damage-wave interaction coefficients for simplified geometries and materials.[23,24]

However, in a real SHM application for composite aircraft structures, in which GW propagation is direction dependent and where there are various three-dimensional geometric complexities and environmental/operational factors acting together, it is not realistic to rely on pure GW mode analysis. Furthermore, the requirements for minimization of hardware usage, system power consumption, and the influence of the transducer network on structural behaviour[7] make it infeasible to deploy dense transducer networks. Above all, the aforementioned selection approaches are unrealistic if GW-based SHM systems are to reach certification level for commercial aviation, as they do not encompass the full complexity of the coupled physics underlying GW transduction nor do they take multiple damage scenarios into account. In short, the lack of a systematic procedure for selecting/designing the transducer network and excitation signal is a major gap preventing the progress towards certification of GW based SHM systems.

This article presents research on reliability improvement of ultrasonic GW-based SHM of full-scale composite aircraft primary structures. This study proposes a novel methodology to consistently design a PZT transducer network, which is not limited to a single damage size, does not resort to unrealistic usage of guided waves (e.g., Lamb mode selection), and is applicable to a generic full-scale composite aircraft primary structure. This design methodology was based on sensor output, coupled electro-mechanical (E/M) response of the transducer-structure assembly, energy transfer from the bonded PZT transducer to the structure, wavefront coverage of the monitored area, and measurement equipment capabilities. The design methodology was successfully validated by testing the capabilities of the SHM system for diagnostic of BVID of different severities, applied in different locations of a full-scale thermoplastic composite aircraft stiffened panel.

This article is structured in seven sections. Section 2 explains the theoretical principles behind the development of the design methodology. Section 3 starts with a summary of the commonly adopted criteria for selecting the excitation signal and the transducer geometry. After justifying why it is not reliable to use those criteria for a real SHM application with real geometric complexity, the proposed novel SHM system design methodology is presented. Section 4 reports the implementation of the proposed design methodology for a full-scale composite aircraft primary structure. Section 5 describes the setup used for the experimental validation of the proposed design methodology. The results of the validation tests are then presented and discussed in Section 6, and the article ends with the main conclusions and contributions in Section 7.

2 | THEORETICAL BASIS

2.1 | Total sensor output

The performance of an SHM system, it influenced by the signal-to-noise ratio of sensor response. Therefore, one should look at the total GW response of a sensor as a function of frequency, as reported in previous studies.[9,15,17,25] For SHM transducer network design purposes, the wavelength solutions of the Rayleigh-Lamb wave equation for the structure

should be taken into account, together with the shape of the PZT transducer and the influence of the actuator on the sensor. Because it is desired to use circular transducers for wavefront omnidirectionality, the formulation presented by Sohn and Lee[17] for the sensor output voltage, V_o, is adopted here. Then, by following the same logic as Raghavan and Cesnik,[15] $|V_o|$ is inversely proportional to the sensor radius, that is, the smaller the sensor radius, the higher the sensor output voltage. On the other hand, $|V_o|$ also has a harmonic dependence on the actuator radius. Therefore, if the effect of both the actuator radius and frequency is to be assessed, then $|V_o|$ can be written as being directly proportional to the harmonic function $f(\xi^S, \xi^A, a)$ on the right-hand side of

$$|V_o| \propto \left| a\left[\sum_{\xi^S}\xi^S J_1\left(\xi^S a\right) + \sum_{\xi^A}\xi^A J_1\left(\xi^A a\right)\right]\right| = f\left(\xi^S, \xi^A, a\right), \tag{1}$$

where J_1 is the Bessel function of Order 1, a is the actuator radius, and ξ^S and ξ^A are the wavenumbers of symmetric and antisymmetric Lamb wave modes, respectively (which in turn depend on their frequency). By evaluating the periodic behaviour of this function, it is possible to determine at which frequency the sensor output voltage reaches a maximum for a certain actuator size.

2.2 | Electro-mechanical response of PZT transducer

The analysis of a piezoceramic transducer must include the study of its E/M behaviour coupled with the mechanical response of the structure to which it is attached because the dynamics of bonded transducer differs considerably from the free condition. [26] During excitation, the piezoceramic may undergo two different types of extreme states, resonance, and antiresonance. The first is characterized by a sudden and pronounced increase in electrical current, accompanied by greatly amplified vibration, which may lead to rupture and/or disruption of the material. This occurs when the admittance tends to infinity, and the impedance approaches zero. The second state corresponds to the opposite situation when the admittance drops to zero, and the impedance tends to infinity, resulting in almost no electrical current being converted to mechanical response. There is a very narrow frequency window where it is possible to obtain very high amplitude GW signals at the resonance. Furthermore, the points of resonance and antiresonance typically occur very close to each other, with an unstable transitory regime, which is detrimental for reliable SHM applications, where it is desired to have a steady generation of GW signals without any perturbations. Therefore, the unstable transitory regime of the resonance/antiresonance should be avoided.

The admittance of a PZT transducer can be calculated according to Giurgiutiu[26]

$$Y(\omega) = i\omega C\left\{1 - k_p^2\left[1 - \frac{(1+\nu_a)J_1(\gamma a)}{\gamma a J_0(\gamma a) - [(1-\nu_a) - \beta(1+\nu_a)]J_1(\gamma a)}\right]\right\}, \tag{2}$$

where a is the radius, C is the electrical capacitance, k_p is the planar electromechanical coupling coefficient, ν_a is the Poisson's ratio of the piezoceramic material, J_0 is the Bessel function of order 0 and $\gamma = \omega/c_{p,pzt}$ with ω being the angular frequency and $c_{p,pzt}$ the bulk pressure wave speed in the piezoceramic material. Because this equation is derived for the bonded transducer condition, it includes the effect of the structure through the ratio of the dynamic stiffness of the structure to that of the PZT, $\beta = k_{str}(\omega)/k_{pzt}$. The value of dynamic stiffness for the PZT transducer is considered to be independent of frequency and can be computed according to formulation given by Giurgiutiu.[26] In the case of the structure, the dynamic stiffness, k_{str} is calculated according to the formulation presented by Giurgiutiu and Zagrai.[27,28] Because those equations take structural vibration modes into account, values for the modal damping were taken from literature.[29,30] The impedance Z is equal to the multiplicative inverse of Y, that is, $Z = 1/Y$.

The resonance points can be found by calculating the zeros of the denominator of Equation (2), whereas the antiresonance points can be obtained by computing the zeros of the entire expression inside the curly brackets of Equation (2).

2.3 | Energy transfer from the PZT transducer to the structure

The shear lag model of the bonding layer between the piezoceramic transducer and the structure derived by Giurgiutiu[9] can be used to perform an energy balance of the entire actuation system. For an SHM application, it is important to

maximize the energy transfer from the actuator to the structure. According to the shear lag model and following the notation adopted by Giurgiutiu,[31] the part of the energy generated by piezoelectric transduction that is transmitted to the host structure, W_{str}, can be approximately calculated by

$$W_{str} = \frac{\alpha\psi}{(\alpha+\psi)^2}\left(\frac{1}{2}E_a\varepsilon_{ISA}^2 t_a 2a\right)\cdot I(\Gamma a), \tag{3}$$

where E_a and t_a are the Young's modulus and thickness of the PZT transducer, respectively, $\varepsilon_{ISA} = -d_{31} \times (V/t_a)$ is the strain induced by a voltage V on the PZT, $I(\Gamma a)$ is the bond efficiency factor, ψ is the 2D relative stiffness coefficient between structure and PZT and α is a shear coefficient, which depends on the stress, strain, and displacement distributions across the plate thickness.[31] The bond efficiency factor in turn depends on the parameter Γ defined for the 2D shear-lag model, as presented by Giurgiutiu.[31]

If W_{str} is normalized by the total induced-strain energy generated through piezoelectric transduction, $W_{ISA} = (1/2)E_a\varepsilon_{ISA}^2 t_a 2a$, then the portion of that energy, which is transmitted to the structure becomes a function of PZT thickness, for a certain PZT diameter. Therefore, the maximum of the normalized energy transmitted to the structure is a useful way to obtain a preliminary value for the theoretically optimal actuator thickness.

2.4 | Measurement equipment capabilities

The selection of frequency and transducer size should also take into account the capabilities of the waveform generator. Although amplification of the excitation signal may be employed, if the waveform generator cannot be operated at its maximum allowable voltage, then it is not possible to maximize the voltage at the terminals of the actuator. Therefore, the waveform generator could be considered as the limiting element in the GW test setup, and the maximum allowable electrical current should be derived from maximum allowable voltage of the waveform generator.

The waveform generator can only generate up to a certain level of voltage, V, which has to be transmitted through a channel with a specific impedance, Z. This imposes a maximum limit on the electrical current, I, that can be supplied to the circuit, according to Ohm's law $V = I \times Z$. If the electrical current required by the circuit downstream of the waveform generator is above the maximum value that can be supplied, then the waveform generator will automatically adapt the generated voltage in order to reduce the current. This occurrence could prevent the waves from being generated with the highest possible amplitude, which in turn affects the signal-to-noise ratio and the quality of the measurements. Therefore, the chosen frequency/actuator diameter combination should allow the corresponding electrical current to be below the maximum allowable current for the waveform generator. In other words, if the highest possible voltage amplitude can be transmitted with an electrical current below the maximum allowable value, then the frequency/actuator diameter combination can be used for the operation of the transducer.

In addition to that, it is also important to pay attention to two other constraints. First, the maximum allowable electric field for the piezoceramic material should be respected. Second, the digital oscilloscope should be able to operate at a sampling frequency suitable for accurate acquisition of ultrasonic signals (e.g., 10 times the centre frequency).

2.5 | PZT transducer thickness effects

The sensor output response is directly proportional to its thickness.[17] Hence, a thicker PZT is in principle more beneficial, from a sensing point of view. From an actuation perspective, the actuation electrical current $I = YC$ depends on the transducer radius, a and the transducer thickness t_a. This thickness influence is included through the capacitance of the transducer, as described by

$$C = \varepsilon_{33}^T \frac{A}{t_a} = \varepsilon_{33,r}^T \varepsilon_0 \cdot \frac{\pi a^2}{t_a}, \tag{4}$$

where A is the surface area of the PZT and the product of the relative dielectric constant and the free-space permittivity, $\varepsilon^T{}_{33,r}\,\varepsilon_0$, defines the dielectric constant of the PZT material $\varepsilon^T{}_{33}$. In this case, the thinner the PZT, the higher the capacitance and the higher the actuation electrical current. So although lower thicknesses promote the generation of a higher actuation voltage (through Ohm's law), the required electrical current might be above the capabilities of the waveform generator (as described in the previous subsection).

3 | DESIGN METHODOLOGY

3.1 | Previous approaches

According to the literature referenced in Sections 1, the usually adopted approach for selecting the excitation frequency content and the PZT transducer geometry can be summarized as follows:

a) GW mode of interest should be as nondispersive as possible
b) Higher order GW modes should be avoided
c) Frequency should allow mode interaction with damage to be detected
d) In conjunction with (a) and (b), the minimum distance resolvable by the mode of interest should be close to the minimum damage size to be detected.

All these criteria are based on the ideal scenario of time-domain discrimination between specific GW modes for extracting signal features. However, that is not a realistic assumption in a real SHM application for composite structures, where the scatter from multiple geometric complexities and material anisotropy prevent the recognition of individual modes. Therefore, criterion (a) should be dropped. Criterion (b) should also be abandoned as one of the main guidelines if the residual time trace is used, as only the difference between states matters. Moreover, although the interference of higher order modes with the fundamental modes can potentially conceal wave features containing information about damage, it can still be argued that at some frequencies the presence of higher order modes might be advantageous for damage diagnostic, depending on their mode shapes.[32] The concept behind criterion (c) (i.e., the higher the frequency, the smaller the wavelength) is important to keep in mind, although the relationship between wavelength and damage size is (partially) lost when frequencies around, or slightly beyond, the cut-off is excited. At those points, the wavelength of higher order modes is quite long, which makes wave-damage interaction weak. So criterion (c) does not seem usable. The reasoning behind criterion (d) is again only valid for a pure mode, which, as mentioned before, does not hold true for a real SHM application. Additionally, none of the aforementioned criteria takes into account the working principles of GW piezoelectric transduction.

Alongside with the design criteria, it is important to take into account mode conversion and direction-dependent GW propagation caused by material anisotropy when designing a GW-SHM system for composite structures. There are interdigital configurations capable of generating ultrasonic GW directionally that take advantage of predominant excitation of one mode over another.[18,33-35] However, when propagating in composite structures with real geometric complexity, the predominantly generated GW mode would undergo mode conversion at different structural features and become inevitably coupled with the other modes possible at the excited frequency band,[36] preventing mode selective sensing with piezoelectric transducers. More importantly, the use of mode selective, directional actuators would only exacerbate the direction-dependent characteristics of GW propagation and would not enable a complete coverage of the area to be monitored.

3.2 | Proposed design methodology

In order to address this challenge, a novel methodology is proposed for designing the excitation frequency content and the transducer geometry more systematically. Instead of assuming single mode analysis, the aim is to optimize the response and operation of the transducer in conjugation with the measurement equipment, namely, by focusing on the physical principles explained in Section 2. The selection criteria are formulated below.

A. The PZT sensor output function should have at least one local maximum in a frequency bandwidth where only zero-order GW modes can be excited.
B. The PZT sensor output function should have more than only one local maximum. More than one excitation frequency should be tested, in order to explore the detection capability of the network at higher frequencies.
C. The chosen frequencies should not coincide with or be in the close vicinity of, E/M resonances or antiresonances of the bonded PZT transducer.
D. The electrical current required to drive the chosen PZT transducer at the chosen frequency should be below the maximum allowable current for the waveform generator output channels. In other words, the required electrical

current for the chosen PZT transducer, at the chosen frequency, should allow a waveform to be generated with the desired voltage amplitude.

E. The selection of the PZT transducer thickness should take into account the maximization of energy transfer from the actuator to the structure.

3.2.1 | Considerations about the transducer shape

One of the most important characteristics for the transducer network to have operational flexibility is to have interchangeable actuator/sensor functions. In other words, the coverage of the monitored area is maximized if all the GW propagation paths are explored, which in turn can be achieved by using each actuator as sensor and vice versa. Therefore, the PZT transducers should all have the same dimensions and properties, at least within each inspected area.

Furthermore, the wavefront coverage of the monitored area by each individual transducer should also be maximized, and those wavefronts should be (approximately) omnidirectional when generated in (quasi-) isotropic material, in an effort to increase robustness against direction-dependent GW propagation. Additionally, as explained in Sections 3.1 and as highlighted by criterion B, it is useful to have the possibility to excite different frequencies in order to explore different damage sensitivities of GWs. For all the above reasons, it was decided to develop the design methodology based on thin piezoceramic discs.

3.2.2 | Considerations about transducer network configuration

The number and positions of the transducers in the network should be chosen so that there is enough virtual wavefront coverage of the region around each critical area. In other words, the monitored area would be covered most efficiently by the wavefronts emanating from all transducers if they would hypothetically generate ultrasounds omnidirectionally at the same time. By maximizing the virtual wavefront coverage, the cases of anisotropic wave propagation (e.g., wave propagation in composites) are not neglected.

Although this is a criterion simply based on visual evaluation, it is well aligned with the concept of multipath unit-cell network,[37,38] according to which the damage index (DI) converges to its "real" value as the number of relevant wave propagation paths increases. Thus, if the number of propagation paths is increased in a meaningful way for the areas to be monitored, while preventing the network from becoming overly dense, then it is not necessary to solve an actual mathematical optimization problem for defining the transducer placement.

3.2.3 | Considerations about PZT material selection

If the only purpose of the PZT transducer was GW actuation, then the selection of the PZT material should predominantly focus on d_{31}, because it quantifies the induced strain in the in-plane direction (Direction 1, in this case radially) per unit electric field applied in the out-of-plane direction (Direction 3). On the other hand, if the only purpose of the PZT transducer was GW sensing, the selection of PZT material should predominantly focus on g_{31} because it quantifies the induced electric field in Direction 3 per unit stress applied in Direction 1. Because it is desirable to maximize the amount of GW data acquired from the monitored area, it is crucial that the selected PZT material can be used for both sensing and actuation. Hence, it is important that both d_{31} and g_{31} are high. From the materials with the highest $d_{31} \times g_{31}$ product, the one with the highest g_{31} is chosen so that the sensing sensitivity is favored.

3.2.4 | Important design checks

After defining the PZT transducers positioning within the network, it is crucial to check if there is enough space available on the structure for the installation. Finally, the maximum allowable electric field for the PZT material should not be exceeded.

All the steps of the SHM system design implementation are reported in Section 4. First, the PZT transducer material is selected in Subsection 4.1. Then, Subsection 4.2 describes the application of criteria A to E one by one to each structural area to be monitored. Finally, the result of the application of the guidelines for positioning the transducers within the network is shown in Subsection 4.5.

4 | DESIGN IMPLEMENTATION

It should be noted that the design implementation presented in the following subsections was conducted for PZT disc diameters varying from 5 to 30 mm in steps of 5 mm and for PZT thicknesses varying from 0.1 to 1 mm in steps of 0.1 mm.

4.1 | PZT material selection

The values of the piezoelectric charge constant, d_{31} and the piezoelectric voltage constant, g_{31} for the materials available from the selected PZT supplier (APC International, Ltd.) are presented in Table 1. As a result of the application of the guidelines for PZT material selection proposed in Subsection 3.2.4, the chosen material was APC 850.

4.2 | Study of the critical areas

The application of design criteria A and B to structural areas to be monitored required the Rayleigh-Lamb wave solutions to be calculated in the form of dispersion curves. As shown later in Subsection 4.5, most of the transducers were placed on the skin of the stiffened panel. Thus, the dispersion curves were calculated for the skin laminates. Also as explained later in Section 5, three structural areas were selected for this study: Areas 1 and 2 (which have approximately the same thickness and laminate stacking sequence) and Area 3. The phase and group velocity dispersion curves for Areas 1–2 and Area 3 are depicted in Figure 1 and Figure 2, respectively. They were obtained with DISPERSE® 2.0.20a (Imperial College, London) by using the composite elastic properties in Table 2 and the symmetric and quasi-isotropic stacking sequences in Table 3 provided by the panel manufacturer.

TABLE 1 Piezoelectric charge and voltage constants in 31 directions, for the different available piezoceramic materials

Parameter	APC 840	APC 841	APC 850	APC 855	APC 880
$d_{31} \times 10^{-12}$ (m/V)	−125	−109	−175	−276	−95
$g_{31} \times 10^{-3}$ (Vm/N)	−11.0	−10.5	−12.4	−9.0	−10.0
$d_{31} \times g_{31} \times 10^{-15}$ (m^2/N)	1375	1144.5	2170	2484	950

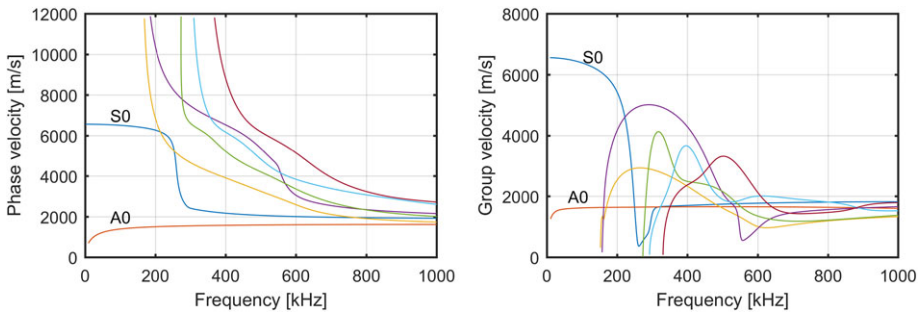

FIGURE 1 Dispersion curves for the skin of Areas 1–2: phase velocity (left) and group velocity (right). For clarity purposes, higher order modes with cut-off frequencies above 400 kHz (i.e., modes that were not excited in any of the tests) are not presented

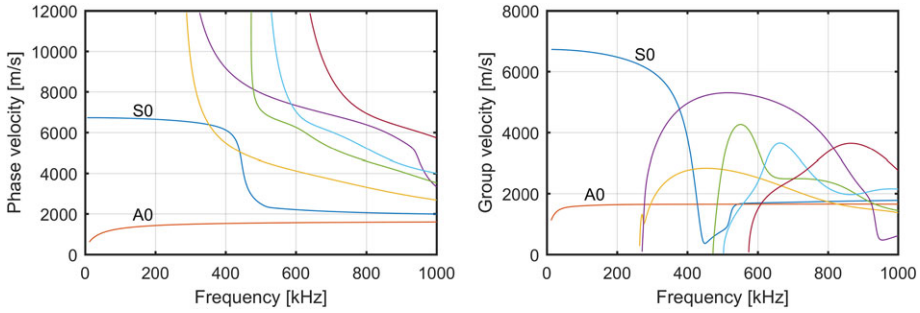

FIGURE 2 Dispersion curves for the skin of Area 3: phase velocity (left) and group velocity (right)

TABLE 2 Elastic properties of the carbon fiber/polyetherketoneketone composite material used for the horizontal stabilizer torsion-box panel

E_{11} (MPa)	E_{22} (MPa)	E_{33} (MPa)	G_{12} (MPa)	G_{13} (MPa)	G_{23} (MPa)	ν_{12}	ν_{13}	ν_{23}	ρ (kg/m^3)
141,000	10,400	10,400	5,460	5,460	3,320	0.3	0.3	0.45	1,560

TABLE 3 Approximate composite ply stacking sequence for the skin of each critical area

Area	Ply thickness (mm)	Ply fiber orientation (°)
1 and 2	$(0.80/0.65/0.53/0.53)_S$	$(0/90/45/135)_S$
3	$(0.55/0.41/0.28/0.28)_S$	

The phase velocity of the fundamental symmetric Lamb mode (S0) at approximately null frequency and the phase velocity of the fundamental antisymmetric Lamb mode (A0) at the last calculated frequency were used as longitudinal and shear bulk wave velocities, c_p, and c_s, respectively, for computing equivalent Poisson's ratio and equivalent Young's modulus, ν_{eq} and E_{eq}, that is, elastic properties of the skin "perceived" by the wavefront, as if the material was isotropic. The relationship between the Lamé constants (λ and μ), density (ρ) for isotropic material, and the bulk wave velocities in

$$\begin{cases} \mu = \rho c_s^2 \\ \lambda = c_p^2 - 2\mu \end{cases}, \tag{5}$$

was used to solve

$$\begin{cases} \mu = \dfrac{E_{eq}}{2(1+\nu_{eq})} \\ \lambda = \dfrac{\nu_{eq} E_{eq}}{(1+\nu_{eq})(1-2\nu_{eq})} \end{cases} \Leftrightarrow \begin{cases} \nu_{eq} = \dfrac{\lambda/2\mu}{2(\lambda/2\mu)+1} \\ E_{eq} = 2\mu(1+\nu_{eq}) \end{cases}. \tag{6}$$

In turn, E_{eq} was used in design criterion E.

Another important quantity for the application of the design criterion A is the frequency bandwidth, as defined in

$$f_{up} = f_c\left(1 + \frac{k_{bw}}{N_{cyc}}\right) \Leftrightarrow f_c = \frac{f_{up}}{\left(1 + \frac{k_{bw}}{N_{cyc}}\right)} \;;\; f_{low} = f_c\left(1 - \frac{k_{bw}}{N_{cyc}}\right). \tag{7}$$

where f_{up} is the frequency bandwidth upper limit, f_c is the excitation centre frequency, f_{low} is the frequency bandwidth lower limit, k_{bw} is the so-called bandwidth parameter, and N_{cyc} is the number of cycles in the excitation pulse. According to Wilcox,[18] the −40 dB bandwidth definition corresponds to a theoretical value of k_{bw} equal to 2.8. However, the computed −40 dB bandwidth of (previously acquired) experimental Hanning windowed excitation tone bursts with centre frequencies ranging from 200 to 750 kHz revealed actual values of k_{bw} approximately equal to 1.9. Taking $k_{bw} = 1.9$ and Equation (7), it is possible to inversely calculate the necessary centre frequency, f_c, if only fundamental Lamb modes are to be generated, that is, if the frequency bandwidth upper limit, f_{up}, is to be at the first cut-off (read from the group velocity dispersion curves because the group velocity is the one at which the pure mode propagates). The values for each area (see Table 4) were calculated for an excitation tone burst amplitude modulated by a Hanning window with N_{cyc} cycles, which has a narrower frequency bandwidth than a simple sinusoid.

TABLE 4 Inversely calculated centre frequency corresponding to a bandwidth upper limit at the first cut-off, for all critical areas

		f_c (kHz)			
Critical area	f_{up} (kHz)	$N_{cyc} = 5$	$N_{cyc} = 10$	$N_{cyc} = 15$	$N_{cyc} = 20$
Areas 1–2	152.52	109.84	127.70	135.03	139.01
Area 3	263.98	190.10	221.03	233.70	240.60

Finally, it is also important to keep in mind that the larger the number of pulse cycles, N_{cyc}, the longer will be the wave groups in the GW response and the more intense will be the interference between them, thereby increasing the probability of losing damage-related information. Hence, it was decided not to go beyond $N_{cyc} = 10$ to keep the duration of the excited wave groups below 0.1 ms.

4.2.1 | Areas 1–2

Criterion A: Single sensor output local maximum

Although sensor output voltage *Vo* is directly proportional to transducer thickness (see Subsection 2.1), Equation (1) does not depend on thickness so neither does the location of the maxima. Hence, it is possible to evaluate criterion A by looking at the graphs independently of the thickness value. As indicated in Table 4, if $N_{cyc} = 5$, then the sensor output function, $f(\xi^S, \xi^A, a)$, should have at least one local maximum around 110 kHz. By looking at Figure 3, it is possible to see that criterion A is satisfied for a PZT diameter, D, of 10 mm with a local maximum at 112 kHz. For PZT diameters of 20 and 30 mm, $f(\xi^S, \xi^A, a)$ at 110 kHz is not at a maximum, but it is in an ascending part of the curve and with a value comparable with the maximum for $D = 10$ mm. If $N_{cyc} = 10$, then $f(\xi^S, \xi^A, a)$ should have a local maximum around 128 kHz. In this case, criterion A is satisfied for $D = 10$, 20, and 30 mm since that frequency falls on or in the close vicinity of a maximum (for $D = 20$ mm there is a maximum at 123 kHz, and for $D = 30$ mm, there is a maximum at 132 kHz). In summary, criterion A is satisfied in the following conditions:

- $D = 10$, 20, and 30 mm, with $N_{cyc} = 10$

Criterion B: Multiple sensor output local maxima

From the plots of Figure 3, it is also possible to see that criterion B is satisfied for transducer diameters above 10 mm. The frequencies of the relevant local maxima for the PZT diameters identified with criterion A are listed in Table 5. In summary, criteria A and B are satisfied in the following conditions:

- $D = 20$ and 30 mm, with $N_{cyc} = 10$

Criterion C: E/M response

For the evaluation of this criterion, transducer thickness must be taken into account. Therefore, the previously identified candidate diameters are taken, and the points of 0 and infinite E/M admittance for each thickness are calculated according to Equation (2). It is relevant to note that the E/M resonance and antiresonance points are always adjacent to each other (as seen in Figure 3, for example). Therefore, it is enough to find the E/M resonance points. For $D = 20$ mm, there are two E/M resonances between 0 and 400 kHz, whereas for $D = 30$ mm there are four.

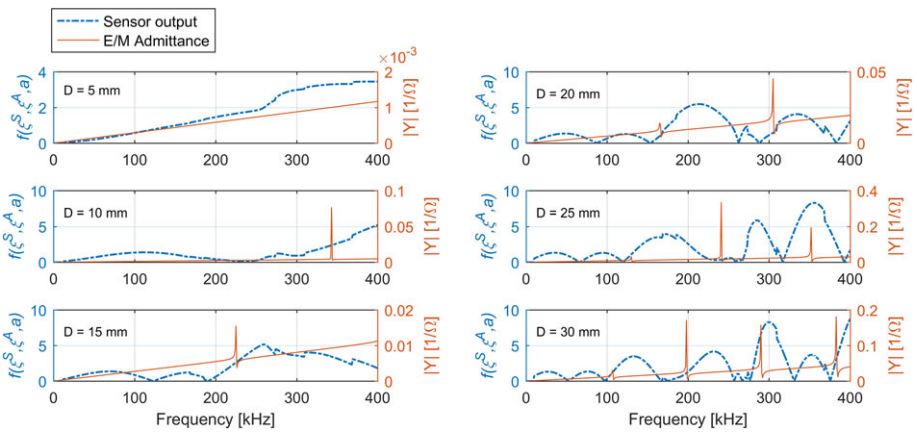

FIGURE 3 Sensor output function and electro-mechanical admittance response (according to Equations 1 and 2, respectively) of PZT transducer with 0.4 mm thickness and different diameters, for Areas 1–2

TABLE 5 Frequencies of the relevant local maxima of the sensor output in Areas 1–2 for the lead zirconate titanate diameters identified with criterion A

	f (kHz)		
Diameter (mm)	**Max. 1**	**Max. 2**	**Max. 3**
20	123	213	335
30	133	232	300

For $D = 20$ mm, all the three relevant sensor output local maxima (see Table 5) are away from any E/M resonances. For $D = 30$ mm, the first two relevant sensor output local maxima are away from any E/M resonances for all transducer thicknesses. The third local maximum only becomes distant from E/M resonances for thicknesses above 0.5 mm. In summary, criteria A, B and C are satisfied in the following conditions:

- $D = 20$ mm, for all thicknesses, with $N_{cyc} = 10$
- $D = 30$ mm, for $t > 0.5$ mm, with $N_{cyc} = 10$

Criterion D: Electrical current limits

The Agilent 33500B waveform generator available in the laboratory has output channels with 50 Ω impedance, and the maximum signal amplitude it can produce is 10 Vpp. Hence, the maximum current that can be supplied by the equipment is 0.1 A. The evolution of electrical current as a function of frequency for $D = 20$ mm and different thicknesses (see Figure 4) was computed as the product of the inverse of Equation (2); in which the capacitance is defined by Equation [4]) and the maximum allowable voltage. It can be seen that only for thicknesses above 0.3 mm is the electrical current at the three previously identified frequencies (see Table 5) below 0.1 A. From similar graphs for $D = 30$ mm, it was observed that only for thicknesses above 0.6 mm is the electrical at the three previously identified frequencies (see Table 5) below 0.1 A. In summary, criteria A to D are satisfied in the following conditions:

- $D = 20$ mm, for $t > 0.3$ mm, with $N_{cyc} = 10$
- $D = 30$ mm, for $t > 0.6$ mm, with $N_{cyc} = 10$

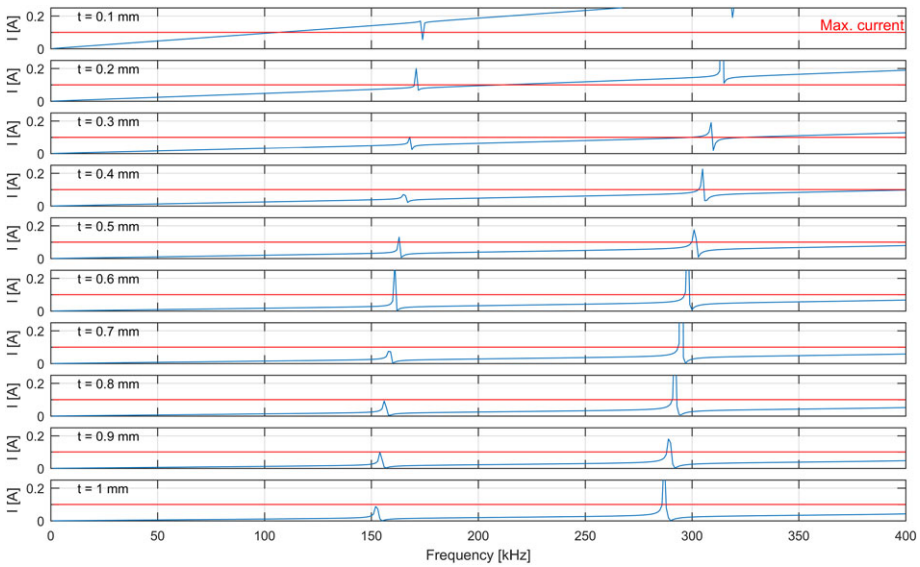

FIGURE 4 Electrical current (computed according to Ohm's law $I = V/Z$, with $Z = 1/Y$ and Y defined in Equation (2)) as function of excitation frequency for $D = 20$ mm and thickness varying from 0.1 to 1 mm on Areas 1–2. The maximum possible current for the waveform generator is represented by a horizontal line in every graph

Criterion E: PZT actuator energy transfer

The normalized energy transmitted to the structure by the PZT actuator calculated according to Equation (3) is plotted in Figure 5 as function of actuator thickness, for actuator diameters ranging from 5 to 30 mm. For the calculations, the shear modulus and thickness of the bonding layer were assumed to be equal to 2 GPa and 10 μm,[9] respectively. Although the curves deviate from each other, they all have an absolute maximum for a thickness equal to 0.3 mm. This means that, in ideal bonding conditions, transmission of ultrasonic energy to the structure is maximized if the transducer is 0.3 mm thick. However, this value falls outside of the design region identified by criteria A to D, which means the adopted PZT thickness does not match the ideal energy transmission conditions. Nevertheless, in the case of $D = 20$ mm, the normalized transmitted energy for $t = 0.4$ mm is only 2.4% lower than for $t = 0.3$ mm, which does not represent a detrimental deviation from the ideal conditions. On the other hand, in the case of $D = 30$ mm, the normalized W_{str} for $t = 0.7$ mm is approximately 16.6% lower than for $t = 0.3$ mm, which is low enough to justify the exclusion of this case from the design space. In summary, criteria A to E are satisfied in the following conditions:

- $D = 20$ mm, for $t = 0.4$ mm, with $N_{cyc} = 10$

4.3 | Final transducer and excitation design

The selected PZT transducer geometry for Areas 1 and 2 is a thin disc with a diameter of 20 mm and a thickness of 0.4 mm. The actuation of ultrasonic GW is to be performed at 123, 213, and 335 kHz, using a 10-cycle tone burst with the amplitude modulated by a Hanning window.

4.3.1 | Area 3

In this subsection, the design implementation for Area 3 is shown directly without further explanations because the procedure for applying the design criteria is the same as that explained in Subsection 4.2.1 for Areas 1–2. The frequencies that enable the application of criterion A can be found in Table 4. The diameters and the frequencies that satisfy criteria A and B for Area 3 can be found in Table 6. Those values are taken as candidates for criteria C to E, until the final design of the transducer and excitation signal is obtained.

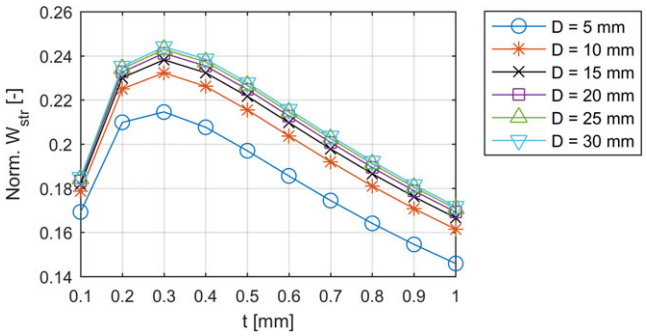

FIGURE 5 Normalized energy transferred by the lead zirconate titanate actuator to the structure (according to Equation (3)) as function of actuator thickness, for actuator diameters varying from 5 to 30 mm on Areas 1–2

TABLE 6 Frequencies of the relevant local maxima of the sensor output in Area 3 for the lead zirconate titanate diameters satisfying criteria A and B

	f (kHz)		
Diameter (mm)	**Max. 1**	**Max. 2**	**Max. 3**
20	112	198	350
25	153	217	280
30	123	176	228

Criterion A: Single sensor output local maximum
In summary, criterion A is satisfied in the following conditions:

- $D = 20$ mm, with $N_{cyc} = 5$
- $D = 25$ and 30 mm, with $N_{cyc} = 10$
- $D = 5$ mm, with $N_{cyc} = 15$

Criterion B: Multiple sensor output local maxima
In summary, criteria A and B are satisfied in the following conditions:

- $D = 20$ mm, with $N_{cyc} = 5$
- $D = 25$ and 30 mm, with $N_{cyc} = 10$

Criterion C: E/M response
In summary, criteria A, B and C are satisfied in the following conditions:

- $D = 20$ mm, for $0.1 \leq t \leq 1.0$ mm, with $N_{cyc} = 5$
- $D = 25$ and 30 mm, for $0.1 \leq t \leq 1.0$ mm, with $N_{cyc} = 10$

Criterion D: Electrical current limits
In summary, criteria A to D are satisfied in the following conditions:

- $D = 20$ mm, for $t > 0.3$ mm, with $N_{cyc} = 5$
- $D = 25$ mm, for $t > 0.4$ mm, with $N_{cyc} = 10$
- $D = 30$ mm, for $t > 0.5$ mm, with $N_{cyc} = 10$

Criterion E: PZT actuator energy transfer
In summary, criteria A to E are satisfied in the following conditions:

- $D = 20$ mm, for $t = 0.4$ mm, with $N_{cyc} = 5$

4.4 | Final transducer and excitation design

The selected PZT transducer geometry for Area 3 is a thin disc with a diameter of 20 mm and a thickness of 0.4 mm. The actuation of ultrasonic GW is to be performed at 112, 198, and 350 kHz, using a 5-cycle tone burst with the amplitude modulated by a Hanning window.

4.5 | Final transducer network configuration

The final transducer network configuration for each area is summarized in Table 7. Figure 6 shows the full-scale horizontal stabilizer torsion box stiffened panel, where it is possible to have a general view of the entire transducer network. Figure 7 and Figure 8 show the detail of the network installation on critical Areas 1–2 and 3, respectively.

4.6 | Design checks

The maximum allowable electric field for APC 850 material is 5 V_{AC}/mil, that is, 5,000 V_{AC}/in = 196.85 V_{AC}/mm. That means the maximum allowable (absolute) voltage for the transducers is 78.74 V. Because the maximum voltage that the waveform generator can supply is 10 Vpp, and the maximum amplification factor available was 1.6, there is no risk of exceeding the allowable limits of the PZT.

TABLE 7 Lead zirconate titanate transducer numbers and their configuration for each critical area

Location	# PZT	PZT no.	Configuration description
Area 1	5	1–5	On the skin, around stringer run out
Area 2	5	6–10	On the skin, around stringer run out
Area 3	4	11–14	On the skin, inboard of outboard rib, around stringer
	2	15, 16	On outboard rib, inboard side of the web, line
	2	17, 18	On the skin, outboard of outboard rib, line

Note. PZT: lead zirconate titanate.

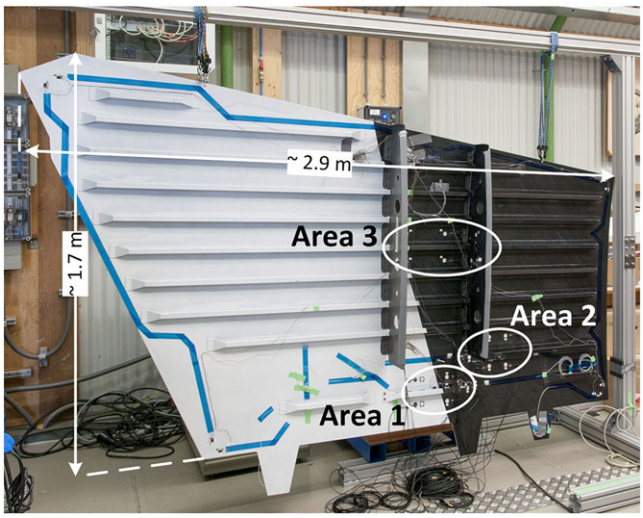

FIGURE 6 Horizontal stabilizer torsion box stiffened panel, with the three critical areas highlighted

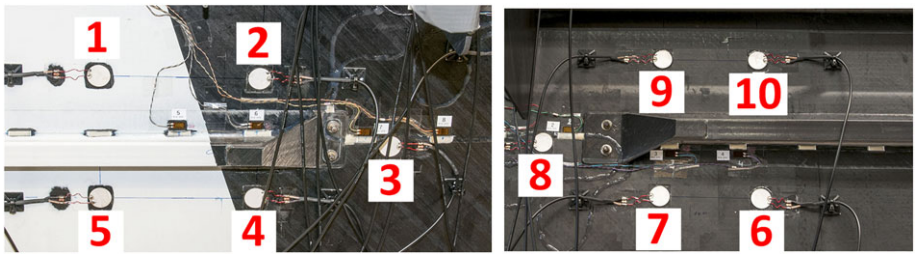

FIGURE 7 Transducer network on critical Area 1 (left) and critical Area 2 (right)

5 | EXPERIMENTAL SETUP

The test specimen was selected as a full-scale horizontal stabilizer torsion box panel entirely made of carbon fiber (CF) reinforced polyetherketoneketone (PEKK), made available by Fokker Aerostructures B.V. for the SHM tasks of the Thermoplastic Affordable Primary Aircraft Structure 2 (TAPAS 2) project. The CF/PEKK composite material properties are listed in Table 2. The component consisted of a coconsolidated stiffened skin with multiple I-stringers in butt-joint configuration and two riveted ribs, as depicted in Figure 9. The panel had a maximum length and width of about 2.9 and 1.7 m, respectively, with skin thickness varying between 1.8 and 8.1 mm and rib thickness between 3 and 3.5 mm.

Three selected critical areas were selected for this study, as shown in Figure 9. The ply stacking sequence for the composite skins was symmetric and quasi-isotropic, as presented in Table 3. The structure was impacted along the stringers, on the outer side of the skin, at the locations indicated in Table 8 and depicted in Figure 9. The impacts were applied by a portable spring-mechanism impactor configured to generate a nominal impact energy of 50 J. Area 3 was impacted a second time with a lower nominal impact energy of 30 J. The projectile head diameter was 12.7 mm, and its mass was around 2.7 kg.

FIGURE 8 Transducer network on critical Area 3

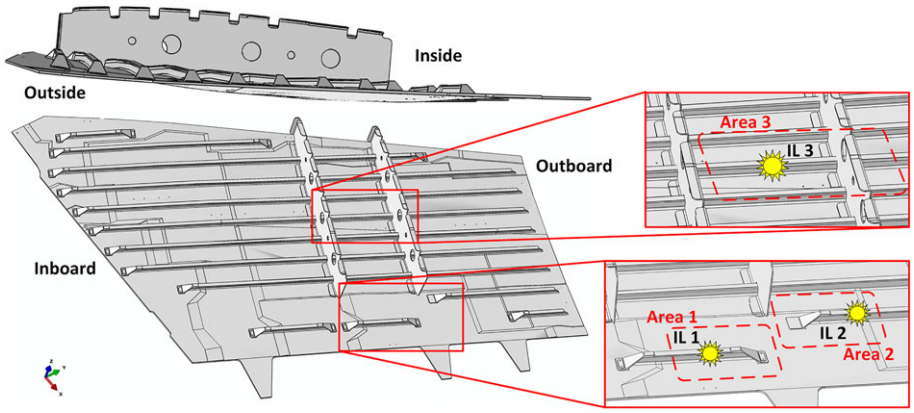

FIGURE 9 General views of the torsion box panel, with highlighted detailed views of the critical areas, with the corresponding impact locations. The impacts were performed on the outside of the skin

TABLE 8 Impact locations along the stringers

Abbreviation	Impact location
IL 1	100 mm from stringer run out
IL 2	100 mm from stringer run out
IL 3	100 mm away from outboard rib

GW measurements were conducted for each area, before and after the impacts. The setup can be seen on the left-hand side of Figure 10: The ultrasonic excitation was produced by an Agilent 33500B waveform generator, amplified by a TTi WA301 wideband amplifier and transmitted to the structure by thin PZT actuator discs (see final design for Areas 1–2 and Area 3 in Subsections 4.2.1.6 and 4.2.2.6, respectively, for details on the material, geometry, and excitation signal); the ultrasonic response was sensed by thin PZT sensor discs and acquired by two digital oscilloscopes, PicoScope 4424, and PicoScope 6402A, both connected to a computer. In order to prevent faulty diagnostics, the integrity of the transducer network was also monitored during the entire test campaign, by measuring the E/M susceptance of the PZT transducers with a Hioki IM 3570 Impedance analyzer connected to Hioki L-2000 4-terminal probe, as shown on the right-hand side of Figure 10.

6 | TEST RESULTS AND DISCUSSION

6.1 | Visual inspections

The real impact energies listed in Table 9 were in accordance with the nominal values introduced in the Section 5. It is important to explain that although Impacts 1 to 3 had identical energies and were performed with exactly the same

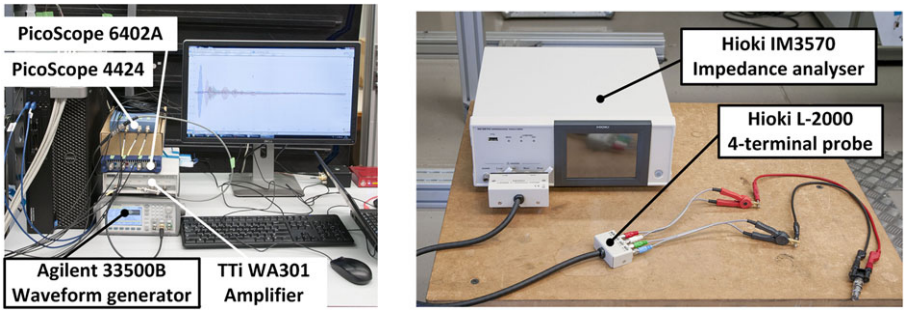

FIGURE 10 Guided wave measurement setup (left) and electro-mechanical susceptance measurement setup (right)

TABLE 9 Real energy of the impacts, skin indentation depth from visual inspection, and the code used to identify the damage created after each impact

Impact no.	Area	Damage code	Indentation depth (mm)	Impact energy (J)
1	3	D3	0.18	49.6
2	1	D1	0.09	49.1
3	2	D2	0.07	47.5
4	3	D3 + D3	0.3	29.5

equipment and projectile, they occurred at different locations of the structure, where different arrangements of the panel stiffening elements impose different boundary conditions. This is a relatively realistic low-energy impact scenario, in which the size and severity of the produced barely-visible damages were not fully under control.

Visual inspections of the impacted areas revealed two types of BVID features. One was shallow indentations at the impact locations (see Table 8 in the Section 5), only perceptible from certain viewing angles and with depths ranging from 0.07 up to 0.3 mm (see Table 9). The other one was a small, irregular crack in the stringer filler across the impact location, which only occurred for Impact Number 1 (on Area 3) and was difficult to visually measure. Both occurrences are depicted in Figure 11.

6.2 | Nondestructive testing

Ultrasonic nondestructive testing performed at a frequency of 5 MHz with an Olympus OmniScan MX unit connected to a phased-array roller probe revealed internal damages at the stringer-skin interface of different severities and sizes. The C-scans obtained for Areas 1–2 and Area 3 are depicted in Figure 12 and Figure 13, respectively. The comparison of the C-scans in Figure 12a and Figure 12b shows damage after impact on Area 1 (D1) as a few spots of low reflectivity (about 20%). In Figure 12c, the damage after impact on Area 2 (D2) is more clearly visible than in the aforementioned case with

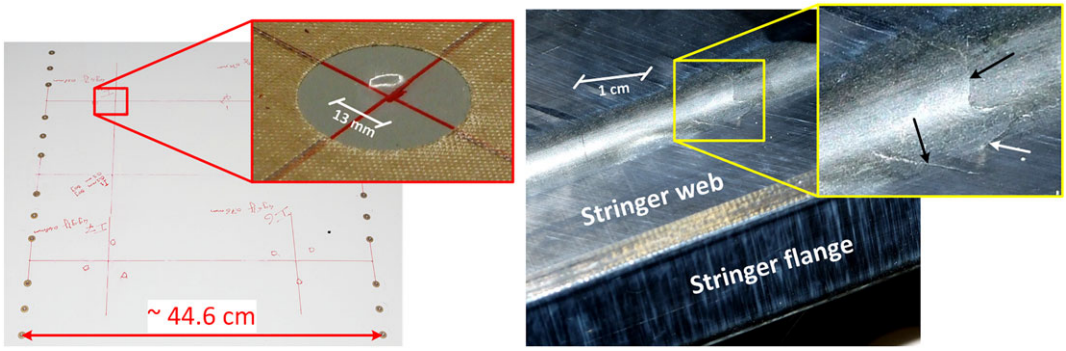

FIGURE 11 Barely-visible damages after first impact on Area 3: indentation (left) and stringer filler crack (right), with irregular shape indicated by arrows

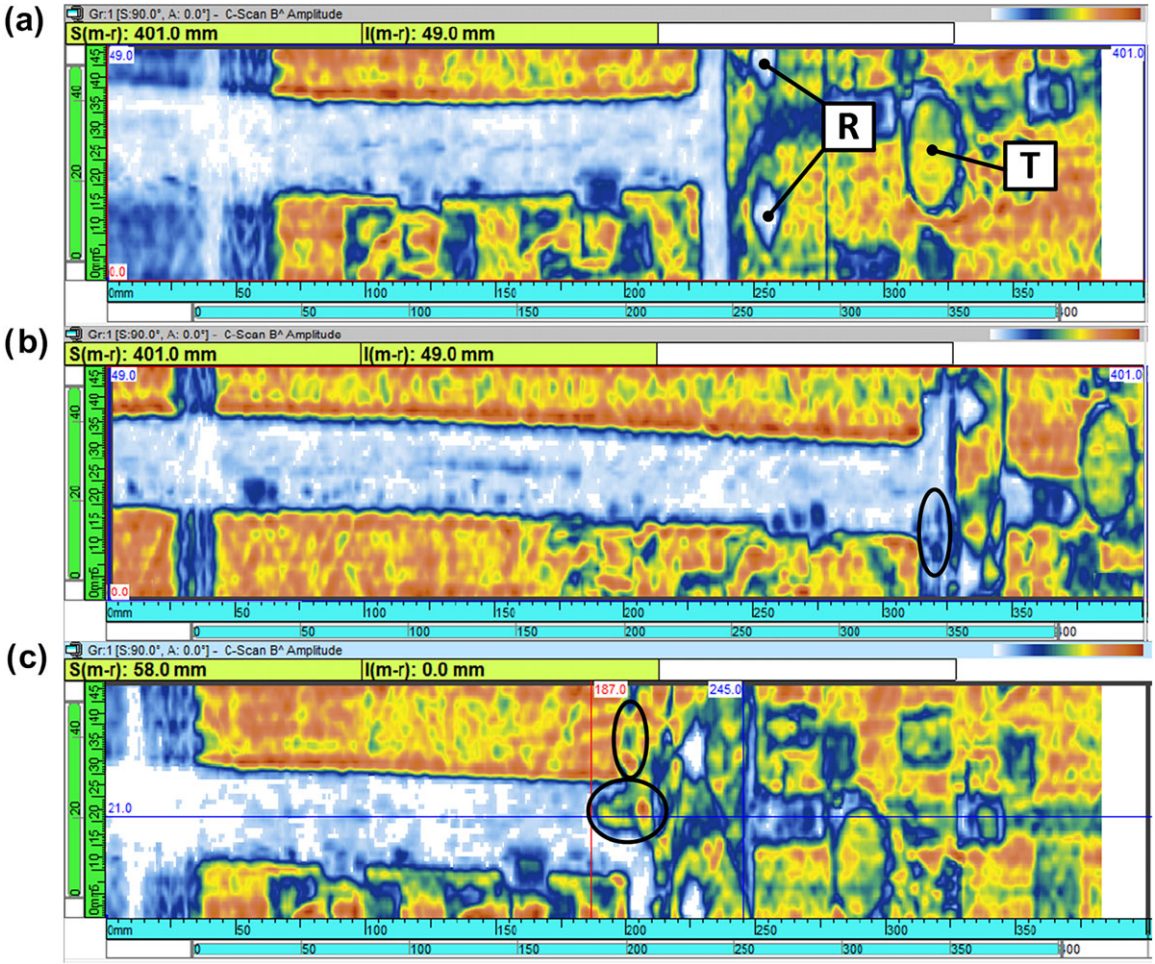

FIGURE 12 Ultrasonic C-scans of stringer run outs: (a) reference, (b) after impact at Area 1, and (c) after impact at Area 2. The reflectivity changes attributed to damage are highlighted by ellipses. The elements with legend in the reference C-scan (a) are R—Rivets, T—PZT transducer (see Figure 7 for a clearer geometry identification)

a reflectivity around 70–80% but covering only an area of approximately 350 mm^2 along the centre front of the stringer and extending for about 10 mm along the stringer run-out bond edge. It is interesting to note that, although the energy of the impact at Area 2 was lower than that of the impact at Area 1, the internal features of damage D2 appeared to be larger and more severe than those of D1. By combining this observation with the differences in indentation depth read from Table 9, it is possible to grasp the effect of different boundary conditions on the damage generated by impacts with identical energy.

The damage after the first impact on Area 3 (D3) can be unambiguously identified when Figure 13a and Figure 13b are compared, as there is a clear delamination running along the stringer-skin interface, with a length and an area of approximately 164 and 2,952 mm^2, respectively. Additionally, there are other damage features on the sides of the stringer, which could be related to the irregular filler crack depicted in Figure 11. When comparing C-scans obtained after the first and second impacts on Area 3, Figure 13b and Figure 13c, respectively, it is not possible to observe any relevant difference, even though it was possible to identify a slight increase in indentation depth, as registered in Table 9.

6.3 | Structural health monitoring

The GW signals were processed with the continuous wavelet transform using the Morlet wavelet in order to filter out the frequencies outside the 20–1,000 kHz band. The filtered signals for each propagation path p were then Fourier transformed to the frequency domain and used to compute the root-mean-square error ($RMSE_f$; based on a combination of two indexes presented in previous research[5,39]), as defined in

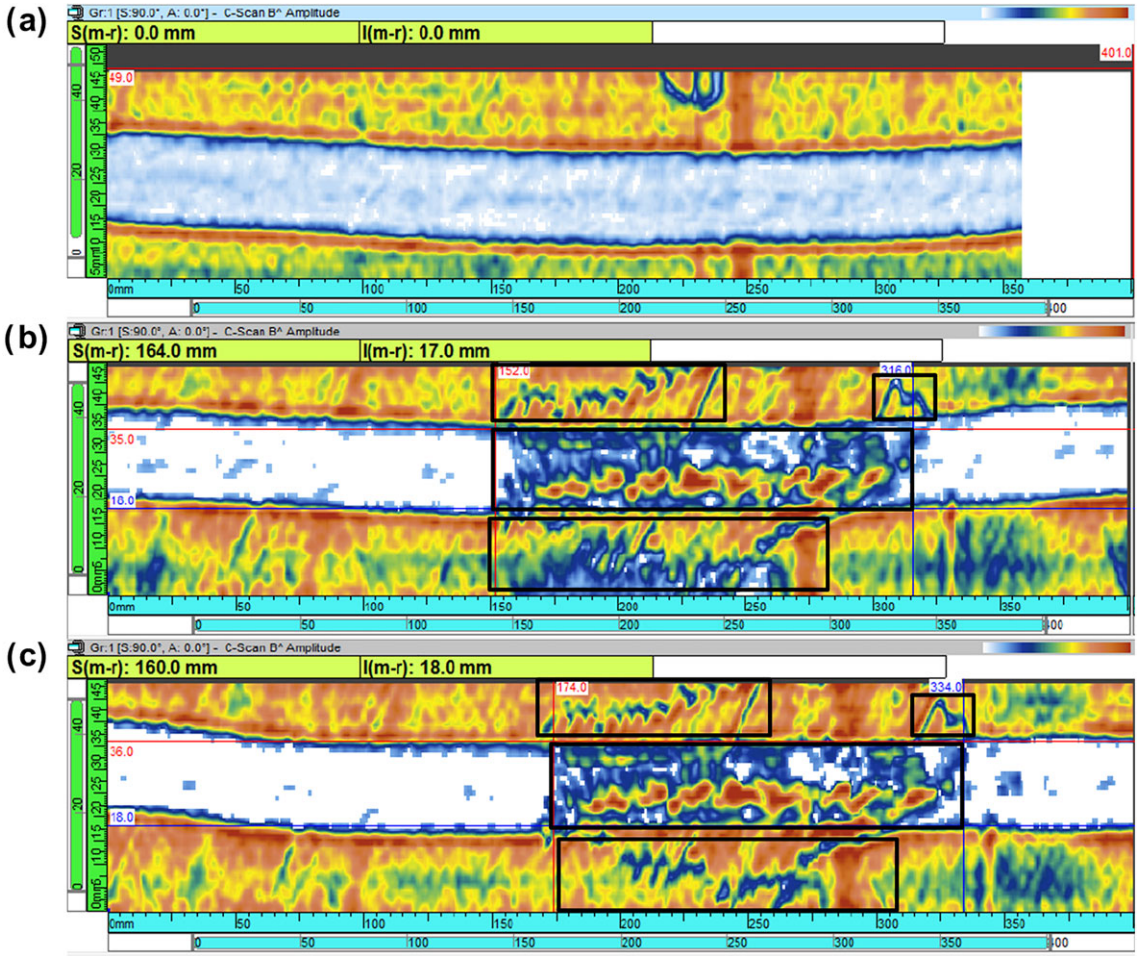

FIGURE 13 Ultrasonic C-scans of stringer at Area 3: (a) reference, (b) after first impact, and (c) after second impact. The reflectivity changes attributed to damage are highlighted by rectangles

$$DI_p = RMSE_f = \sqrt{\frac{\sum_{i=1}^{n}\left[s(f)_i - s(f)_i^0\right]^2}{\sum_{i=1}^{n}\left[s(f)_i^0\right]^2}},\ p \in N, \tag{8}$$

where $s(f)^0$ and $s(f)$ are the frequency domain baseline and new-state signals, respectively and n is the number of signal sample points. This index corresponds to the standard deviation of the differences between the signals, thereby being a measure of the signal shape change.

The multipath unit-cell network concept (introduced earlier in Subsection 3.2.3) was applied, and the final DI value for a monitored area was computed as the weighted average of all N paths in that area, as defined by

$$DI = \sum_{p=1}^{p=N} w_p DI_p, \text{ with } w_p = \frac{DI_p}{\sum_{p=1}^{p=N} DI_p}. \tag{9}$$

The application of this concept makes the DI independent of propagation path orientation with respect to the structural elements in the monitored area, thereby generating a DI value, which corresponds to a measure of the total change in the scatter field.

The final DI values for each state and frequency are plotted in Figure 14, in which excitation Frequencies 1, 2, 3 were 123, 213, 335 kHz for Areas 1–2 and 112, 198, 350 kHz for Area 3. All frequencies have the same trend with a consistent monotonic increase from nondamaged to damage D3, and an almost constant value from D3 to D3 + D3. The DI values for damage states D1 and D2 increase with frequency, whereas those for states D3 and D3 + D3 remain

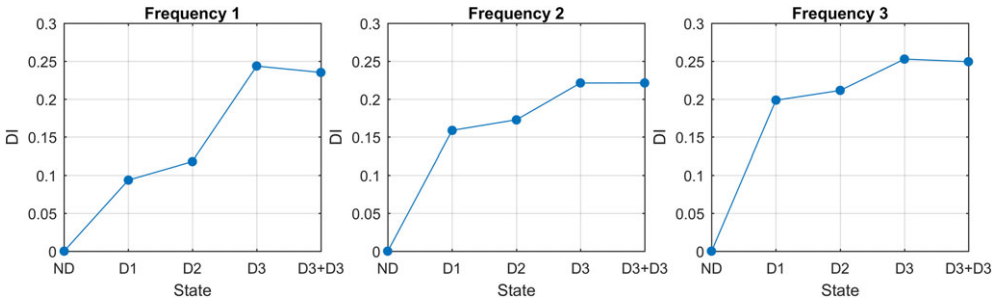

FIGURE 14 Weighted-average DI values for each state at Frequency 1 (left), 2 (centre), and 3 (right). Frequencies 1, 2, 3 were 123, 213, 335 kHz for Areas 1–2 and 112, 198, 350 kHz for Area 3

approximately the same at the three frequencies. Thus, damage states D1, D2, and D3 were unambiguously detected and quantified by the transducer network. In fact, the detection of D1 is clearer than by observing the ultrasonic C-scan presented in Figure 12b. The DI values for damages D3 and D3 + D3 are comparable with the values obtained by Monnier[39] for similar BVID in similar full-scale composite component monitored at similar frequencies, thereby confirming the accuracy of quantification. However, contrary to previous research,[40] the transducer network showed equal sensitivity to BVIDs with considerably different areas.

It is interesting to observe that there is a slight reduction in DI from D3 to D3 + D3 for Frequency 1 and an even slighter one for Frequency 3. As previously explained, the adopted DI measures change in the frequency spectrum, whether due to the appearance/disappearance of frequency components or due to the increase/decrease of magnitude at existing frequency components. These changes are the consequence of interference between new reverberations created by the presence of damage. However, if those reverberations are partially attenuated within damage features, then the difference of the sensed signals with respect to the baseline condition becomes less pronounced. Even though the ultrasonic C-scan performed after the second impact on Area 3 (see Figure 13c) did not reveal any noticeable difference with respect to the first impact, there might be some increase in delamination opening without increase in length[41] causing the aforementioned partial attenuation. This could explain the slight DI reductions observed. In order to test this hypothesis, the energy ratio defined in

$$\Delta E_r = \frac{|E[s_1(t)] - E[s_0(t)]|}{E[s_0(t)]} \tag{10}$$

was computed for each path of Area 3 for states D3 and D3 + D3, where $s_0(t)$ and $s_1(t)$ are the time-domain baseline and new-state signals, respectively and $E[s(t)]$ is the time-domain signal energy calculated through trapezoidal numerical integration of the squared amplitude over time. The difference between the two damage states was taken for 112 and 350 kHz and is presented in Table 10 and Table 12, respectively.

In order to identify the relevance of the propagation paths, their weighting factors based on the energy ratio for damage D3 at 112 and 350 kHz are presented in Table 11 and Table 13, respectively. The combined analysis of Table 10 and

TABLE 10 Variation of energy ratio between damage states D3 and D3 + D3 for all propagation paths within Area 3 at 112 kHz

PZT #	11	12	13	14	15	16	17	18
11	0	↓−0.0099	↑0.0230	↓−0.0008	↑0.0104	↓−0.0397	↑0.0314	↓−0.1166
12	↓−0.0135	0	↓−0.0059	↑0.0116	↑0.0307	↓−0.0652	↑0.0307	↓−0.2859
13	↑0.0283	↓−0.0239	0	↑0.0113	↑0.0834	↑0.0033	↓−0.1772	↓−0.0084
14	↑0.0024	↑0.0098	↑0.0067	0	↑0.0337	↓−0.0203	↓−0.0114	↑0.0394
15	↑0.0014	↑0.0246	↑0.0642	↑0.0349	0	↑0.0191	↑0.0352	↑0.2006
16	↓−0.0278	↓−0.0527	↓−0.0062	↓−0.0174	↑0.0185	0	↑0.0810	↑0.0534
17	↑0.0572	↑0.0133	↓−0.1252	↓−0.0193	↑0.0645	↑0.0743	0	↓−0.0343
18	↓−0.0628	↓−0.2186	↓−0.0334	↑0.0307	↑0.1751	↑0.0506	↓−0.0355	0

Note. PZT: lead zirconate titanate.

TABLE 11 Weighting factors for all propagation paths within Area 3, based on the energy ratio for damage state D3 at 112 kHz. Path relevance is proportional to filled area in circle icon

PZT #	11	12	13	14	15	16	17	18
11	0	0.0076	0.0045	0.0020	0.0287	0.0207	0.0030	0.0155
12	0.0067	0	0.0014	0.0043	0.0356	0.0059	0.0062	0.0958
13	0.0029	0.0023	0	0.0005	0.0280	0.0182	0.0576	0.0200
14	0.0020	0.0050	0.0019	0	0.0315	0.0126	0.0419	0.0059
15	0.0293	0.0361	0.0299	0.0323	0	0.0052	0.0021	0.0024
16	0.0202	0.0046	0.0192	0.0125	0.0051	0	0.0037	0.0068
17	0.0024	0.0081	0.0534	0.0441	0.0012	0.0063	0	0.0316
18	0.0137	0.0910	0.0221	0.0062	0.0043	0.0067	0.0310	0

Note. PZT: lead zirconate titanate.

TABLE 12 Variation of energy ratio between damage states D3 and D3 + D3 for all propagation paths within Area 3 at 350 kHz

PZT #	11	12	13	14	15	16	17	18
11	0	↑0.0344	↓−0.0783	↑0.0148	↑0.1630	↑0.0363	↑0.0037	↓−0.0678
12	↑0.0393	0	↓−0.0996	↑0.0168	↓−0.0464	↑0.1490	↓−0.0078	↓−0.2443
13	↓−0.0980	↓−0.0781	0	↑0.0287	↓−0.3240	↑0.0848	↓−0.0353	↑0.0194
14	↑0.0212	↑0.0224	↑0.0211	0	↓−0.0257	↓−0.0900	↓−0.0108	↑0.0172
15	↑0.2545	↓−0.0776	↓−0.0833	↑0.0344	0	↑0.0233	↓−0.1487	↑0.0775
16	↑0.2377	↑0.1342	↑0.0595	↓−0.0742	↑0.0278	0	↑0.0134	↑0.0746
17	↓−0.0254	↓−0.0241	↓−0.0417	↓−0.0145	↓−0.1519	↑0.0049	0	↓−0.0164
18	↑0.0580	↓−0.2789	↑0.0174	↑0.0075	↑0.1073	↑0.0837	↓−0.0201	0

Note. PZT: lead zirconate titanate.

TABLE 13 Weighting factors for all propagation paths within Area 3, based on the energy ratio for damage state D3 at 350 kHz. Path relevance is proportional to filled area in circle icon

PZT #	11	12	13	14	15	16	17	18
11	0	0.0019	0.0061	0.0003	0.0237	0.0064	0.0182	0.0061
12	0.0024	0	0.0077	0.0045	0.0047	0.0921	0.0195	0.0525
13	0.0082	0.0070	0	0.0072	0.0297	0.0095	0.0032	0.0208
14	0.0003	0.0038	0.0094	0	0.0234	0.0260	0.0434	0.0192
15	0.0261	0.0062	0.0133	0.0128	0	0.0077	0.0263	0.0162
16	0.0150	0.0707	0.0111	0.0223	0.0076	0	0.0250	0.0047
17	0.0212	0.0199	0.0060	0.0509	0.0239	0.0257	0	0.0040
18	0.0046	0.0548	0.0231	0.0205	0.0137	0.0052	0.0044	0

Note. PZT: lead zirconate titanate.

Table 11 indicates noticeable ΔE_r reductions at 112 kHz for the three most relevant paths, 12–18, 13–17, and 18–12. At 350 kHz, Table 12 and Table 13 indicate relevant reductions for paths 12–18, 14–17, 17–14, and 18–12, as well as for other less relevant paths. However, because there is an increase for the most relevant paths, 16–12 and 12–16, the drop in final DI is not as marked as at 112 kHz. Therefore, although the hypothesis cannot be entirely proven, it seems valid to say that a fraction of the energy scattered by the damage D3 + D3 does not arrive at the sensors. Nevertheless, the SHM system was able to detect the presence of damage D3 + D3 through DI increases for individual propagation paths.

A sparser transducer network configuration was also tested in order to evaluate the robustness of the placement approach. The sparser configuration consisted of actuator on PZT 01 and sensor on PZTs 07, 10, 11, and 18, thereby covering the three critical areas. The tested frequency was 123 kHz. In this case, the selected baseline condition, IA0, was the state after the first impact on Area 3, D3. The $RMSE_f$ for each propagation path is depicted on Figure 15. The main contribution for the $RMSE_f$ value for state D3 + D3 + D1 (IA1 in Figure 15) for Path 1–7 is due to the presence of damage D1 (apart from the influence of the reflections coming from Area 3) because Area 1 is the only region crossed by that propagation path (recall the relative PZT positions within the transducer network shown in Figure 6 to Figure 8). The same can be said for the Path 1–10, for which the detected value is just slightly higher than for Path 1–7 because PZT 10 is closer to Area 3 than PZT 07. For the Path 1–18, the propagating wavefront crosses Areas 1 and 3. So the $RMSE_f$ value reflects the presence of both D3 + D3 and D1, almost reaching the double of the value acquired for Path 1–7. Finally, although Path 1–11 crosses Areas 1 and 3, the wavefront arriving at the sensor captures the presence of both D3 + D3 and D1 only through reflections. As a result, the $RMSE_f$ value lies in between those acquired for Paths 1–7 and 1–18. After the impact on Area 2 (state IA2 in Figure 15), the accumulation of damage D2 is detected by all the paths of the sparse network, with a sensitivity, which is in agreement with the explanation given for the cumulative state D3 + D3 + D1. When Figure 15 is compared with the ultrasonic C-scans in Figure 12b and in Figure 13c, it is possible to see that the diagnostic of the cumulative state D3 + D3 + D1 by the ultrasonic GW based SHM system is more unambiguous.

Therefore, the SHM system was able to detect the cumulative BVID without needing an optimization of the transducer network configuration for each damage size, while using an excitation frequency, which was not an optimum for the entire covered region.

For the sake of result transparency, Figure 16 shows the evolution of the degradation of all PZT transducers as a function of time (i.e., data set number within the sequence of tests). In this case, the transducer network degradation is quantified by the complement of the coefficient of correlation ($DI_{PZT} = 1—CC$) between each E/M susceptance curve (recorded at each E/M scan of test campaign) and the one at the start.[42-44] The E/M susceptance was measured between 50 and 500 kHz. As it is visible from the graph, the PZT transducer damage indicator remains very low and with almost

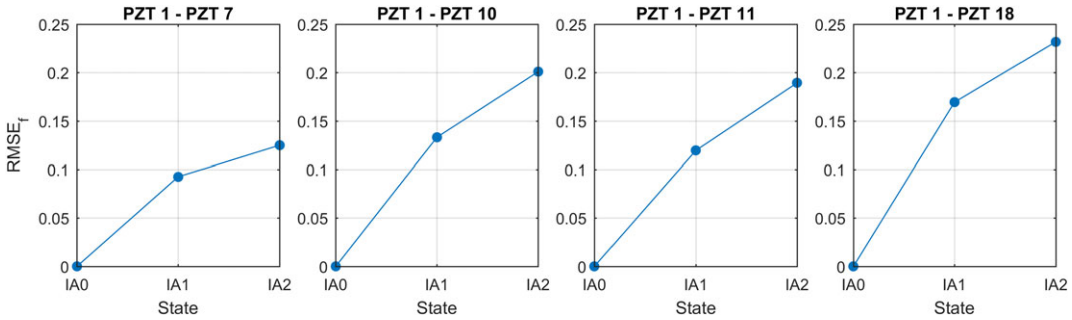

FIGURE 15 $RMSE_f$ for sparse transducer network at 123 kHz. IA0 = D3 (reference for inter-area tests); IA1 = D3 + D3 + D1; IA2 = D3 + D3 + D1 + D2

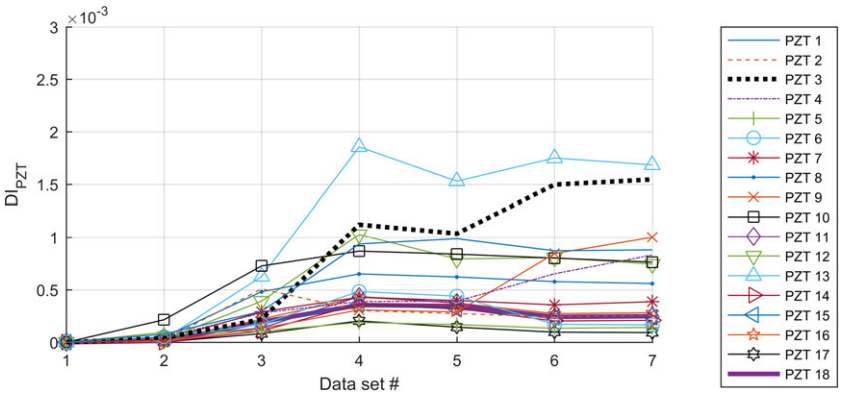

FIGURE 16 Evolution of the transducer network degradation during the test campaign. The damage indicator for the transducer network, DI_{PZT}, is calculated as the complement of the coefficient of correlation CC ($DI_{PZT} = 1—CC$)

no relevant variation, which confirms that the DI variations for GW signals acquired by the SHM system from the critical areas were not caused by degradation of the transducer network.

As this discussion reaches an end, it is relevant to mention that the design methodology proposed in this article can be useful both for researchers developing their own GW-SHM systems and for users of commercially available system solutions who want to have a well-informed decision on their purchase.

7 | CONCLUSIONS

This article presented a novel methodology to systematically design an ultrasonic GW-based structural health monitoring (SHM) system, which is not limited to a single damage size, does not resort to unrealistic usage of guided waves (e.g., Lamb mode selection), and is applicable to a generic full-scale composite aircraft primary structure. The proposed set of criteria for defining the excitation frequency content, geometry, and positioning of PZT transducers was based on the optimization of the sensor output, coupled electro-mechanical (E/M) response of the transducer-structure assembly, energy transfer from the bonded PZT transducer to the structure, wavefront coverage of the monitored area, and measurement equipment capabilities. Moreover, the choice of PZT material reflected the need for having transducers with interchangeable function between actuator and sensor.

In order to validate the design criteria, a test campaign was conducted on a full-scale horizontal stabilizer torsion box panel entirely made of carbon fiber reinforced thermoplastic material. BVID of different severities was applied to different critical locations of the structure, and GW measurements were performed before and after each state. The integrity of the transducer network was also recorded by measuring the E/M susceptance, in order to avoid faulty diagnostics.

According to the ultrasonic C-scans of the critical areas, the length of the BVID-related stringer-skin delamination ranged from a couple of millimeters up to 164 mm. All the different BVID were detected by the SHM system. The obtained DI values for the largest BVID were comparable with the values for similar damage size obtained by other researchers, thereby confirming the accuracy of damage quantification. However, contrary to those other researchers, the SHM system designed according to the novel methodology proposed in this article was equally sensitive to both large and small BVID. In fact, the DI values for Area 1 allowed a less ambiguous detection than the ultrasonic C-scan, where the damage showed up only as a few spots with low reflectivity of about 20%.

Additionally, it was also possible to detect and quantify the accumulation of successive BVID, both in normal and sparse transducer network configurations, thereby showing that it is not necessary to perform a transducer network optimization for each different damage scenario. The performance of the SHM system in the detection of accumulated BVID at Area 3 even surpassed that of the ultrasonic C-scan, where the second impact did not produce any noticeable reflectivity difference with respect to the first impact.

Therefore, it can be concluded that the proposed methodology for consistently designing the transducer network has the potential for maximizing the diagnostic effectiveness of a GW-SHM system, as it enabled the mission accomplishment for a variety of damage sizes in different critical areas of the structure. To really assess that potential, a probability-of-detection study of the system should be conducted in order to understand how the transducer network parameters affect the diagnostic reliability.

It is important to state the physics used in each design criterion is not novel. However, to the authors' knowledge, it is the first time such physical criteria have been used in a fully integrated way in order to develop a procedure for systematically designing a PZT transducer network for GW-SHM without depending on damage size tuning or relying on single guided mode analysis. The successful validation of the novel design methodology represents an important first contribution for the certification of GW-SHM systems, ultimately bringing them one step closer to implementation in condition-based maintenance programmes for commercial aviation.

ACKNOWLEDGEMENTS

The authors would like to thank Frank Grooteman from the Netherlands Aerospace Centre (NLR) for his collaboration before, during, and after the test campaign on the torsion box panel and Pieter Lantermans from Fokker Aerostructures B.V. for providing the torsion box panel. Last but not least, the authors would like to show their gratitude to Lourens Prikken and Dion Baptista, also from the NLR, for their support during the installation of the piezoelectric transducers on the torsion box panel.

FUNDING STATEMENT

This research is part of the Thermoplastic Affordable Primary Aircraft Structure 2 project, financed by the Netherlands Enterprise Agency of the Ministry of Economic Affairs.

ORCID

Pedro Ochôa https://orcid.org/0000-0001-5422-0402
Roger M. Groves https://orcid.org/0000-0001-9169-9256

REFERENCES

1. Wenk L, Bockenheimer C. Structural health monitoring: a real-time on board 'stethoscope' for condition-based maintenance. Airbus Technical Magazine - Flight Airworthiness Support Technology. August, 2014: 22.
2. Gardiner G. Structural health monitoring: NDT-integrated aerostructures enter service. *Composites World* 31 July, 2015. https://www.compositesworld.com/articles/structural-health-monitoring-ndt-integrated-aerostructures-enter-service. Accessed July 25, 2018.
3. Smith RA. *Report from the Workshop on NDT and SHM Requirements for Aerospace Composites*. Northampton: BINDT; February 2016.
4. Su Z, Ye L, Lu Y. Guided lamb waves for identification of damage in composite structures: a review. *J Sound Vib*. 2006;295(3-5):753-780.
5. Su Z, Ye L. *Identification of Damage Using Lamb Waves: From Fundamentals to Applications*. Berlin-Heidelberg: Springer; 2009.
6. Mitra M, Gopalakrishnan S. Guided wave based structural health monitoring: a review. *Smart Mater Struct*. 2016;25(5):053001.
7. ARP6461:2013–09. Guidelines for implementation of Structural Health Monitoring on fixed wing aircraft.
8. Croxford AJ, Wilcox PD, Drinkwater W, Konstantinidis G. Strategies for guided-wave structural health monitoring. *Proc R Soc A*. 2007;463(2087):2961-2981.
9. Giurgiutiu V. *Structural Health Monitoring with Piezoelectric Wafer Active Sensors*. 2nd ed. Academic Press – Elsevier; 2014.
10. Su Z, Ye L. Selective generation of lamb wave modes and their propagation characteristics in defective composite laminates. *Proc Instn Mech Engrs*. 2004;218(2):95-110.
11. Ramadas C, Balasubramaniam K, Joshi M, Krishnamurthy CV. Interaction of guided lamb waves with an asymmetrically located delamination in a laminated composite plate. *Smart Mater Struct*. 2010;19:1-11.
12. Sherafat MH, Guitel R, Quaegebeur N, Lessard L, Hubert P, Masson P. Guided wave scattering behavior in composite bonded assemblies. *Compos Struct*. 2016;136:696-705.
13. Ng CT, Veidt M. Scattering of the fundamental anti-symmetric lamb wave at delaminations in composite laminates. *J Acoust Soc Am*. 2011;129(3):1288-1296.
14. Memmolo V, Monaco E, Boffa ND, Maio L, Ricci F. Guided wave propagation and scattering for structural health monitoring of stiffened composites. *Compos Struct*. 2018;184:568-580.
15. Raghavan A, Cesnik CES. Modeling of piezoelectric-based lamb-wave generation and sensing for structural health monitoring. *Proc SPIE*. 2004;5391:419-430.
16. Giurgiutiu V. Tuned lamb wave excitation and detection with piezoelectric wafer active sensors for structural health monitoring. *J Intell Mater Syst Struct*. 2005;16(4):291-305.
17. Sohn H, Lee SJ. Lamb wave tuning curve calibration for surface-bonded piezoelectric transducers. *Smart Mater Struct*. 2010;19(1):015007-12.
18. Wilcox PD. *Lamb wave inspection of large structures using permanently attached transducers*. London: Imperial College London; 1998.
19. Zhao X, Gao H, Zhang G, et al. Active health monitoring of an aircraft wing with embedded piezoelectric sensor/actuator network: I. Defect detection, localization and growth monitoring. *Smart Mater Struct*. 2007;16(4):1208-1217.
20. Moix-Bonet M, Wierach P, Loendersloot R, Bach M. Damage Assessment in Composite Structures Based on Acousto-Ultrasonics – Evaluation of Performance. In: Wölcken P, Papadopoulos M, eds. *Smart Intelligent Aircraft Structures (SARISTU)*. Switzerland: Springer; 2016:617-629.
21. Wandowski T, Malinowski PH, Ostachowicz WM. Circular sensing networks for guided waves based structural health monitoring. *Mech Syst Sig Process*. 2016;66:248-267.
22. Salmanpour MS, Khodaei ZS, Aliabadi MH. Transducer placement optimisation scheme for a delay and sum damage detection algorithm. *Struct Contol Health Monit*. 2017;24(e1898):2-20.
23. Shen Y, Giurgiutiu V. WaveFormRevealer: an analytical framework and predictive tool for the simulation of multi-modal guided wave propagation and interaction with damage. *Struct Health Monit*. 2014;13(5):491-511.
24. Shen Y, Giurgiutiu V. Combined analytical FEM approach for efficient simulation of lamb wave damage detection. *Ultrasonics*. 2016;69:116-128.

25. Pohl J, Willberg C, Gabbert U, Mook G. Experimental and theoretical analysis of lamb wave generation by piezoceramic actuators for structural health monitoring. *Exp Mech*. 2012;52(4):429-438.
26. Giurgiutiu V. PWAS resonators. In: Giurgiutiu V, ed. *Structural Health Monitoring with Piezoelectric Wafer Active Sensors*. 2nd ed. Academic Press – Elsevier; 2014.
27. Giurgiutiu V, Zagrai AN. Characterization of piezoelectric wafer active transducers. *J Intell Mater Syst Struct*. 2000;11(12):959-975.
28. Giurgiutiu V, Zagrai AN. Embedded self-sensing piezoelectric active sensors for on-line structural identification. *Trans ASME*. 2002;124:116-125.
29. Kang YK, Park HC, Hwang W, Han KS. Prediction and measurement of modal damping of laminated composite beams with piezoceramic sensor/actuator. *J Intell Mater Syst Struct*. 1996;7(1):25-32.
30. Chennamsetti R, Hood A, Guruprasad S, Roy S, Joshi M. Damping ratios of pristine composite beam and constrained layer damped composite beam of equal stiffness. *Int J Precis Eng Manuf*. 2013;14(9):1655-1660.
31. Giurgiutiu V. Coupling of PWAS transducers to the monitored structure. In: Giurgiutiu V, ed. *Structural Health Monitoring with Piezoelectric Wafer Active Sensors*. 2nd ed. Academic Press – Elsevier; 2014.
32. Kundu T, Maji A, Ghosh T, Maslov K. Detection of kissing bonds by lamb waves. *Ultrasonics*. 1998;35(8):573-580.
33. Jin J, Quek ST, Wang Q. Design of interdigital transducers for crack detection in plates. *Ultrasonics*. 2005;43(6):481-493.
34. Petculescu G, Krishnaswamy S, Achenbacj JD. Group delay measurements using modally selective lamb wave transducers for detection and sizing of delaminations in composites. *Smart Mater Struct*. 2008;17(1):015007-9.
35. Schmidt D, Sinapius M, Wierach P. Design of mode selective actuators for lamb wave excitation in composite plates. *CEAS Aeronaut J*. 2013;4(1):105-112.
36. Putkis O, Dalton RP, Croxford AJ. The anisotropic propagation of ultrasonic guided waves in composite materials and implications for practical applications. *Ultrasonics*. 2016;65:390-399.
37. Janapati V, Yadav SK, Kumar A, Ikegami R, Habtour E. Fatigue crack quantification approach based on multi-path unit-cell concept in sensor network. Paper presented at: 8th European workshop on structural health monitoring; July 5-8, 2016; Bilbao, Spain
38. Yadav SK, Chung H, Kopsaftopoulos F, Chang FK. Damage quantification of active sensing acousto-ultrasound-based SHM based on a multi-path unit-cell approach. Paper presented at: 11th International Workshop on Structural Health Monitoring; September 12–14, 2017; Palo Alto, CA, USA.
39. Monnier T. Lamb waves-based impact damage monitoring of a stiffened aircraft panel using piezoelectric transducers. *J Intell Mater Syst Struct*. 2006;17(5):411-421.
40. Eckstein B, Moix-Bonet M, Bach M, Fritzen CP. Lamb wave interaction at debondings due to impact damage in complex stiffened CFRP structures. *Proc SPIE*. 2017; 10170;(101701Q):1-14.
41. Richardson MOW, Wisheart MJ. Review of low-velocity impact properties of composite materials. *Composites Part A*. 1996;27(12):1123-1131.
42. Buethe I, Moix-Bonet M, Wierach P, Fritzen CP. Check of piezoelectric transducers using the electro-mechanical impedance. Paper presented at: 7th European workshop on structural health monitoring; July 8-11, 2014; Nantes, France
43. Park G, Farrar CR, Di Scalea FL, Coccia S. Performance assessment and validation of piezoelectric active-sensors in structural health monitoring. *Smart Mater Struct*. 2006;15(6):1673-1683.
44. Blackshire JL, Cooney AT. Characterization of bonded piezoelectric sensor performance and durability in simulated aircraft environments. *AIP Conf Proc*. 2006;820:1694-1701.

How to cite this article: Ochôa P, Groves RM, Benedictus R. Systematic multiparameter design methodology for an ultrasonic health monitoring system for full-scale composite aircraft primary structures. *Struct Control Health Monit*. 2019;26:e2340. https://doi.org/10.1002/stc.2340